IOP Publishing Journal of Micromechanics and Microengineering
J. Micromech. Microeng. **27** (2017) 075004 (10pp) https://doi.org/10.1088/1361-6439/aa711f

Electrowetting-based microfluidic operations on rapid-manufactured devices for heat pipe applications

Renee S Hale[1] **and Vaibhav Bahadur**[2]

[1] McKetta Department of Chemical Engineering, The University of Texas at Austin, Austin, TX 78712, United States of America
[2] Department of Mechanical Engineering, The University of Texas at Austin, Austin, TX 78712, United States of America

E-mail: vb@austin.utexas.edu

Received 5 February 2017, revised 25 April 2017
Accepted for publication 4 May 2017
Published 2 June 2017

Abstract

The heat transport capacity of traditional heat pipes is limited by the capillary pressure generated in the internal wick that pumps condensate to the evaporator. Recently, the authors conceptualized a novel heat pipe architecture, wherein wick-based pumping is replaced by electrowetting (EW)-based pumping of microliter droplets in the adiabatic section. An electrowetting heat pipe (EHP) can overcome the capillary limit to heat transport capacity and enable compact, planar, gravity-insensitive, and ultralow power consumption heat pipes that transport kiloWatt heat loads over extended distances. *This work develops a novel technique for rapid, scalable fabrication of EW-based devices and studies critical microfluidic operations underlying the EHP, with the objective of predicting the key performance parameters of the EHP*. Devices are fabricated on a printed circuit board (PCB) substrate with mechanically-milled electrodes, and a removable polyimide dielectric film. The first set of experiments uncovers the maximum channel gap (1 mm) for reliable EW-based pumping; this parameter determines the heat transport capacity of the EHP, which scales linearly with the channel gap. The second set of experiments uncovers the maximum channel gap (375 microns) at which EW voltages can successfully split droplets. This is an important consideration which ensures EHP operability in the event of unintentional droplet merging. The third set of experiments demonstrate and study EW-induced droplet generation from an open-to-air reservoir, which mimics the interface between the condenser and adiabatic sections of the EHP. The experimental findings predict that planar, water-based EHPs with a (10 cm by 4 mm) cross section can transport 1.6 kW over extended distances (>1 m), with a thermal resistance of 0.01 K W^{-1}.

Keywords: electrowetting, heat pipe, rapid manufacturing, digital microfluidics, droplet pumping, droplet generation

S Supplementary material for this article is available online

(Some figures may appear in colour only in the online journal)

1. Introduction

Electrowetting (EW) (Mugele and Baret 2005) has received significant research attention in the past two decades, with applications that include lab-on-chip devices, optical lenses, displays, boiling heat transfer enhancement, and thermal management (Hayes and Feenstra 2003, Zhou *et al* 2009, You and Steckl 2010, Ding *et al* 2012, Peng *et al* 2014, Russell *et al* 2014, Pan *et al* 2015, Foat *et al* 2016, Shahriari *et al* 2016). Electrowetting is based on an effective reduction in the energy

of a solid–liquid interface by applying a potential difference between an electrically conducting droplet resting on a dielectric and an underlying ground electrode (Lee *et al* 2002, Quilliet and Berge 2001, Pollack *et al* 2002, Cho *et al* 2003, Mugele and Baret 2005, Bahadur and Garimella 2008, Kumari *et al* 2008, Heikenfeld *et al* 2011, Choi *et al* 2012, Nelson and Kim 2012, McHale *et al* 2013, Chen and Bonaccurso 2014). EW has been used for pumping droplets and for related microfluidic operations such as creating, mixing, and splitting droplets.

A significant number of studies have analyzed EW-based droplet motion. Motion is achieved by sandwiching a droplet between two flat plates. Individually addressable control electrodes are fabricated lithographically on the bottom plate and then covered by a thin dielectric layer, followed by a hydrophobic layer. By pulsing voltages along the array of individual electrodes on the bottom plate (to set up a traveling electric field), droplets can be moved continuously. It is noted that the top plate serves as the electrical ground. EW-based droplet motion can also be achieved in a single-plate configuration, where the bottom plate is patterned with both the ground and activation electrodes. Single-plate systems facilitate rapid droplet mixing, easier access to dispense liquids, and the ability to manipulate large droplets (Park and Lee 2009, Jebrail *et al* 2012). However, two-plate systems can accomplish a broader range of droplet manipulation operations (dispensing, splitting, moving, and merging).

1.1. Description of an electrowetting heat pipe

Electrowetting has attracted the attention of the thermal management community, since a moving droplet can absorb heat by convective and evaporative means (Baird and Mohseni 2008, Mohseni and Baird 2007). Researchers have studied hot spot thermal management using EW-induced droplet motion (Pamula and Chakrabarty 2003, Bahadur and Garimella 2008, Kumari and Garimella 2011, Cheng and Chen 2012, Migliaccio and Garimella 2013).

Recently, Hale and Bahadur (2015) introduced and analyzed a novel heat pipe architecture that relies on EW-based pumping. Heat pipes transport heat passively by cyclically evaporating and condensing a working fluid. Conventional heat pipes use the capillary pressure generated by a wick to move liquid from the condenser to the evaporator. Such heat pipes are performance limited by the maximum flow rate that can be sustained by the wick (Faghri 1995). Transporting large heat loads over long distances is challenging since the fluid (and heat) transport capacity varies inversely with length.

The central concept underlying the electrowetting heat pipe (EHP) (Hale and Bahadur 2015) is the replacement of the heat pipe wick with EW-based pumping to transport condensate as microliter droplets to the evaporator. The condensate does not flow through a high flow resistance porous wick, and the pumping power is not limited by the capillary pressure. The fundamental capillary limit to heat transport capacity of conventional heat pipes can thus be overcome by the EHP.

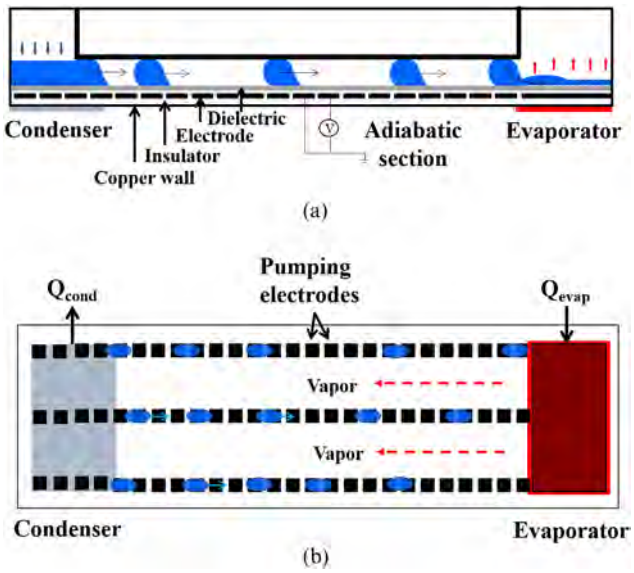

Figure 1. Schematic of an electrowetting heat pipe (EHP) showing (a) evaporator, condenser and adiabatic sections (with separate liquid and vapor channels) in the side view, and (b) top view. © 2015 IEEE. Reprinted, with permission, from Hale and Bahadur (2015).

Figure 1 shows top and side views of a conceptual planar EHP, which consists of separate liquid and vapor conduits with a common evaporator and condenser at the ends. Vapor and liquid travel in separate channels to prevent entrainment. At the condenser, liquid droplets are generated and moved towards the evaporator using EW-based pumping. At the evaporator, the droplets spread into a thin film (under the influence of an EW voltage) to facilitate evaporation and continue the cycle. It is noted that the droplet pumping will not stop if droplets merge to form larger droplets. Instead, the control sequence of the electrodes can be altered so that smaller droplets are 'pinched' out from the larger droplet when the voltage cycles; these can continue moving towards the evaporator.

Hale and Bahadur (2015, 2016) modeled various operational aspects of the EHP and compared EHP performance with various active and passive heat transport devices. Analysis indicates that EHPs with a cross section footprint of 10 cm (width) by 4 mm (thickness) can transport 1.5 kW over extended distances (>1 m) with water as the working fluid, while offering a thermal resistance of 0.01 K W^{-1} and consuming microwatts of power. A comparison with other equivalent heat pipe architectures indicates that the EHP can transport more than twice the heat transport capacity of other heat pipes. Other benefits include a planar form factor, non-dependence on gravity, opportunities for active control, compatibility with multiple working fluids, and the absence of moving parts.

1.2. Unique requirements of an EW platform for EHP applications

The objective of the present work is to characterize the key microfluidic operations that influence the operation of the EHP. *While EW-based microfluidic operations have been widely*

Table 1. Summary of rapid-manufactured EW devices reported in literature (including present work).

Authors	Substrate and electrode fabrication	Dielectric layer (thickness)	Hydro-phobic layer	Top plate	Electrode size; channel gap	Maximum voltage
Abdelgawad and Wheeler (2008)	Chemically etched PCB	Saran wrap (15 μm)	Rain-X	ITO-coated glass	2 × 2 mm; 150 μm channel gap	800 V AC
Li *et al* (2014)	PCB (no details on fabrication)	Saran wrap (15 μm)	Peanut oil	ITO-coated glass	2 × 2 mm; Channel gap not reported	400 V AC
Jain *et al* (2015)	PCB (no fabrication details)	PDMS (35 μm)	PDMS	None	2 × 2 mm and 2.5 × 2.5 mm; no channel gap (single-plate)	400 V DC
Phongsomboon *et al* (2011)	Chemically etched PCB	Polyester tape (63 μm)	Saran wrap/ Rain-X	None, grounded by copper tape strip	2 × 2 mm; no channel gap (single-plate)	800 V AC
Abdelgawad and Wheeler (2007)	Chemically etched PCB	PDMS (up to 40 μm)	Teflon-AF	Copper with PDMS and teflon-AF	1 × 1 mm; 75 μm channel gap	300 V AC
Hale and Bahadur (present)	PCB, routed with PCB mill	Polyimide (12.5 μm)	CYTOP	ITO-coated glass	2 × 2 mm, 1.5 × 1.5 mm; 125–325 μm	600 V DC

studied, the majority of such studies have targeted lab-on-a-chip (LOC) applications. The EW platform for an EHP, on the other hand, has many unique requirements, which are outlined in this section. Firstly, the heat transport capacity of an EHP is directly proportional to the droplet volume and the number of droplets in the device. Larger channel gaps with the same electrode footprint are therefore desirable. LOC-based EW devices typically have a <500 μm channel gap (Cho *et al* 2002, Pollack *et al* 2002), with droplet volumes being a few microliters or less (Abdelgawad and Wheeler 2008). Abdelgawad and Wheeler (2008) demonstrated EW-based droplet movement of milliliter sized droplets using large electrodes (25 × 30 mm); this shows that droplet pumping can be scaled up. However, a larger electrode footprint will reduce the number of liquid channels for a fixed footprint area of the device. Alternatively, a larger channel gap will result in a larger droplet volume. This work experimentally uncovers the maximum channel gap (for a fixed electrode size) at which droplets can be pumped reliably. This information is used to refine the preliminary EHP architecture proposed by Hale and Bahadur (2015).

Secondly, successful working of the EHP hinges on droplet generation from an open condensate pool into flat plate channels. Past efforts have concentrated on droplet generation from covered reservoirs for LOC applications. Covered-reservoir generation is different than the open-reservoir generation needed for the EHP. Section 3.3 outlines the fundamental differences between open-reservoir and covered-reservoir generation. Cho *et al* (2003) first demonstrated that droplets could be pinched from an open fluid reservoir in air. They found that smaller channel gaps enhanced the necking needed to pinch off the droplets, and that the pinch-off location was inconsistent unless perpendicular side electrodes were used to draw the reservoir liquid away from the necking location. Wang *et al* (2011) discovered that the generated droplet volume depended on the voltage-dependent tail volume at pinch-off. Related research on covered-reservoir generation has focused on lowering droplet volume inconsistency during pinch-off (Ren *et al* 2004, Gong and Kim 2008, Shih *et al* 2011, Liu *et al* 2014, Samiei and Hoorfar 2015) Despite all these advances in droplet generation, no prior study has an indepth focus on open-reservoir droplet generation. This work analyzes droplet generation from an open-reservoir to establish the feasibility of the condenser-adiabatic section interface.

1.3. Need for rapid and scalable manufacturing method

In addition to the microfluidics-related requirements, the EHP also requires a manufacturing technique that is rapid, scalable and low cost. The EHP will be much larger than typical LOC devices, which are usually manufactured via expensive cleanroom-based techniques. Another limitation of most EW manufacturing techniques is that the devices cannot be reused following degradation of the EW dielectric layer or any other reason.

There are recent efforts directed towards rapid and low cost manufacturing of EW devices. Table 1 summarizes the most relevant efforts. Printed circuit boards (PCBs) have been explored as a rapid-manufacturing and inexpensive platform for EW devices (Leiterer *et al* 2015). PCBs consist of an insulating laminate base covered by a thin copper metal layer. Chemical etching with a printed ink mask is the default method of patterning the electrodes into the copper layer (Abdelgawad and Wheeler 2008, Phongsomboon *et al* 2011, Li *et al* 2014). The dielectric layer is the most critical component of EW devices. Common materials like Saran Wrap and Rain-X have been explored as EW dielectric layers and hydrophobic layers, respectively, however the electrode surfaces are not easy to reuse (Abdelgawad and Wheeler 2008, Li *et al* 2014).

The studies in table 1 utilized voltages ranging from 300–800 V (AC and DC voltages) for droplet movement in air (Abdelgawad and Wheeler 2008, Phongsomboon *et al* 2011, Li *et al* 2014). The present work demonstrates droplet movement in air at speeds of up to 10.5 mm s^{-1} using 600 V DC. Previous work also reported droplet splitting and merging, but the maximum channel gap studied was 150 μm (Abdelgawad and Wheeler 2008). This work demonstrates droplet splitting in a range of channel gaps, up to 380 μm. It is noted that this work utilizes higher voltages than those in LOC device studies. It is important to highlight that the EHP is targeted at industrial applications, where high voltages can be accepted, as compared to portable LOC devices.

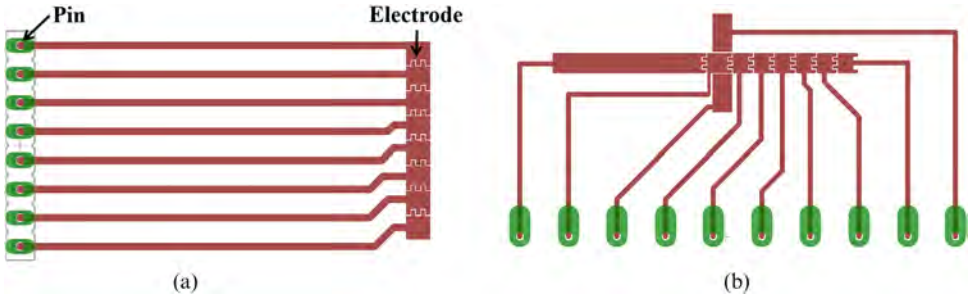

Figure 2. Electrode array architectures used in the present work (a) linear array (2 × 2 mm), (b) linear array (2 × 2 mm) with two additional side electrodes (2 × 4 mm).

2. Methods

2.1. Manufacturing process

This section details the manufacturing process employed in this study and highlights differences from previous efforts. This work used PCBs as the substrate instead of wafers or glass slides (commonly used in lithography-based fabrication of EW devices). The commercial availability and low cost of large sized PCBs are attractive from an EHP standpoint. The novelty in this study lies in the method of creating the electrode patterns. A PCB routing machine was used to physically mill electrode patterns into the copper layer. This provided several advantages over chemical etching, including non-exposure to any chemicals, accurate and precision machining, and the ability for real-time pattern modification. A 12.5 μm thick polyimide layer (CAPLINQ Corporation) was utilized as the EW dielectric. This is the thinnest commercially available polyimide layer that can be attached to the device without the use of spin coating or other deposition techniques. This dielectric layer is thicker than those in LOC systems (~1 μm), which increases the operating voltage. Key benefits of this dielectric layer include its pinhole-free nature, robustness, and high breakdown voltage. All these aspects enhance the reliability and longevity of the device. Importantly, this manufacturing technique ensures easy replacement of the dielectric layer in the event of failure or degradation. This maskless process of making the EW electrode architectures offers flexibility in the placement and thickness of the dielectric and hydrophobic layers.

Electrodes were manufactured on a standard 2.5 mm × 3.8 mm copper-clad PCB substrate using a Cirqoid PCB prototyping machine. Two electrode architectures were created: a single linear array of 2 × 2 mm electrodes, and an array with two additional side electrodes (figure 2). All electrodes were interdigitated by 0.5 mm to facilitate droplet transport. The gaps between electrodes ranged from 0.2–0.3 mm, depending on the routing depth. The gap size could not be smaller than 0.2 mm; this restriction is based on the diameter of the smallest milling tool. Copper traces extended from each electrode to corresponding pins in a linear array near the edge of the board. Electrical pins were soldered into the board and then inserted into a breadboard containing a control circuit to activate individual electrodes.

CYTOP (Bellex International Corporation) was used as the hydrophobic layer on top of the dielectric. CYTOP was spin coated to yield a 1 μm hydrophobic layer. Spincoating conditions were 500 rpm for 10 s followed by 1000 rpm for 20 s. The CYTOP layer was soft baked at 120 °C for 5 min followed by a hard bake at 180 °C for 1 h. To prevent liquid from spreading along the copper traces under an applied voltage, the areas outside the electrodes were masked off during the CYTOP deposition process.

An indium-tin-oxide (ITO)-coated glass slide (Delta Technologies) served as the top plate. After spincoating the slide with CYTOP, the slide was soaked in silicone oil for 12 h. Absorption of silicone oil into the hydrophobic layer reduces hysteresis and the actuation voltage (Gupta *et al* 2011). Silver paint was used to electrically connect the ITO layer to the opposite side of the slide, where a grounding wire was attached without interfering with the channel gap. The channel gap spacing was adjusted by stacking layers of Kapton tape (thickness of each layer is 25 μm). Figure 3 shows the top view of an assembled device.

2.2. Experimental setup

The control circuitry was a set of logic gates to control the high voltage signal to each electrode, similar to the circuit developed by Jang *et al* (2009). Alternative circuits and strategies for controlling the electrodes are detailed in Hong *et al* (2012) and (2013). Presently, Labview was used to send high/low TTL signals for each electrode to a bread board through a National Instruments digital I/O card (NI 9401). Each signal passed through an optocoupler and a transistor on the bread board, which either opened or closed the connection to a high-voltage DC power supply (Matsusada RGE-650-0.1). Each exiting signal then traveled to its corresponding PCB pin location. In the absence of a high-voltage signal, all electrodes and the surrounding PCB were grounded. The experiments involved depositing droplets of deionized water with a pipette and turning on a preset electrode activation sequence. For better optical visualization, food coloring was added to the water. Droplet motion was imaged from the top at 30 fps. The maximum voltage used in the present experiments was 600 V.

The following section describes three sets of experiments. The first set of experiments targets identifying the maximum channel gap at which droplets can be pumped reliably using EW voltages. The second set of experiments identifies the maximum channel gap at which droplets can be split, to establish the upper limit on the channel gap in the EHP. The third

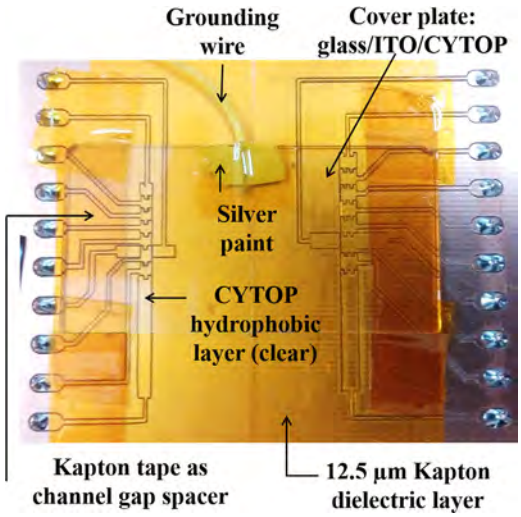

Figure 3. Electrowetting device consisting of a printed circuit board as the bottom plate, with electrodes milled from a copper layer, and with a polyimide film as the dielectric layer.

set of experiments studies EW-induced droplet generation from an open reservoir, which simulates the interface between the condenser and the adiabatic sections of the EHP.

3. Results

3.1. Experiments to estimate maximum channel gap that can sustain EW-induced droplet movement

This section analyzes the effects of switching patterns, droplet sizes, and channel gaps on droplet speed. The objective of these experiments was to establish the limits on droplet size and channel gap. Droplets were moved back and forth across an array of 8 electrodes (figure 2(a)) based on a timed electrode activation pattern. The switching speed was increased in discrete increments until the droplet ceased to show reproducible movement. All experiments were conducted at 600 V.

Droplet movement was initially investigated using three different switching patterns. The single-step pattern (figure 4(a)) produced the slowest speeds, because the droplet struggled to 'catch' on the next activated electrode before the previous electrode deactivated. There was no measurable difference in maximum droplet speeds between the patterns in figures 4(b) and (c). However, based on the recommendation of SadAbadi *et al* (2009), all subsequent experiments were conducted with the pattern shown in figure 4(c).

Droplet transport was evaluated at velocities of 1.05 mm s^{-1}, 2.1 mm s^{-1}, 4.2 mm s^{-1}, 7 mm s^{-1}, and 10.5 mm s^{-1}. The supplementary information includes videos showing droplet movement for four channel gaps with two different droplet sizes each (videos 1–4) (stacks.iop.org/JMM/27/075004/mmedia). Droplets that spanned at least 2 electrodes when stretched by an EW voltage (figure 5(a)) showed higher maximum speeds than droplets that reached less than halfway across the adjacent electrode (figure 5(b)). As an illustration, for a channel gap of 125 μm, the maximum droplet speed increased from 7 mm s^{-1} to 10.5 mm s^{-1} when the nominal droplet length (based on a rectangular box approximation) increased from 1.5 $\times$ to 2.5 $\times$ the electrode length. For the same increase in the length ratio at a 250 μm gap, the maximum speed of the droplet increased from 4.2 mm s^{-1} to 7 mm s^{-1}. Both droplets span multiple electrodes, but the consistency and speed of transfer is higher for the droplet with the larger footprint. This is primarily a consequence of the larger actuation force which scales as square of the footprint radius (Bahadur and Garimella 2006). The increased momentum of the larger footprint droplets also enables it to cross the inter-electrode gap to sustain droplet motion.

Subsequently, experiments were conducted to estimate the maximum channel gap that ensures consistent droplet movement. Droplet motion was analyzed at channel gaps of 125 μm, 250 μm, 625 μm, 1 mm, and 2 mm. Droplet movement failed for a 2 mm channel gap because the weight of the droplet caused it to detach from the top plate. Droplet speeds reached 7 mm s^{-1} for the channel gaps of 1 mm or less. However, the highest speed of 10.5 mm s^{-1} was achieved consistently only with the 125 μm channel gap. This matches the theoretical relationship that a lower channel gap creates a higher driving pressure gradient (Walker and Shapiro 2006, Guan *et al* 2016). Overall, it can be concluded that droplet pumping considerations will allow a maximum channel gap of 1 mm in the EHP.

3.2. Experiments to analyze EW-induced droplet splitting

This section details the experiments to analyze the splitting of droplets as a function of channel gap and voltage. Splitting droplets is essential to continue operation in the event that adjacent droplets combined. The fundamental physics underlying droplet splitting is the creation of a pressure distribution within the droplet such that the center radius of curvature becomes negative and sufficiently severe to cause pinching (Cho *et al* 2003, Walker and Shapiro 2006, Gong and Kim, 2008). Cho *et al* (2003) developed a scaling law for splitting a droplet symmetrically down the middle by deactivating a center electrode and activating the surrounding electrodes. In the present work, experiments were conducted at channel gaps of 125 μm, 250 μm, 375 μm, and 500 μm using 600 V DC. The center electrode was 2 $\times$ 2.5 mm and the adjacent electrodes were 2 $\times$ 4 mm. Droplets successfully split at channel gaps of 125 μm, 250 μm, and 375 μm (figure 6(a)). At a channel gap of 500 μm, significant necking was seen, however the droplet did not split (figure 6(b)). The present work thus demonstrates successful droplet splitting at a maximum channel gap of 375 μm. It is noted that Cho *et al* (2003) did not achieve successful splitting of a 0.9 μl droplet in a 300 μm channel gap on similar sized electrodes. However, that work used a lower electric field (0.083 V μm^{-1}) as compared to the 1.6 V μm^{-1} field presently. Overall, these experiments suggest that droplet splitting considerations establish the upper limit on the channel gap in the EHP instead of droplet pumping considerations.

Additional experiments were conducted to determine the relationship between the droplet splitting speed and applied voltage for a fixed channel gap. Knowledge of the splitting kinetics is important to enable rapid splitting in the event of

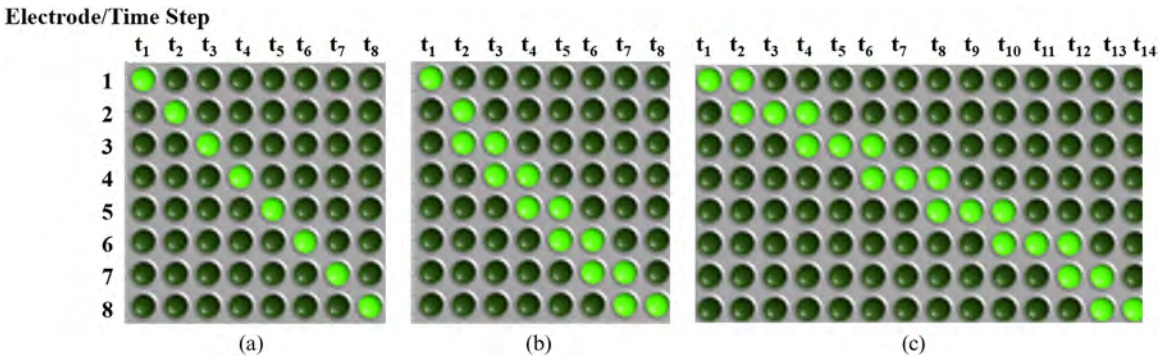

Figure 4. Electrode activation patterns utilized in the present work. (a) Single-step, (b) double-step, (c) step-and-hold. Note: green indicates the activated electrodes.

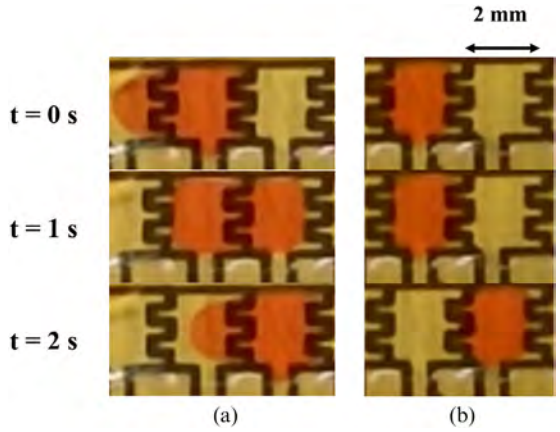

Figure 5. Images showing droplet motion in a 125 μm channel gap. Droplet volume is (a) 1.5 μl and (b) 0.75 μl. Droplet speeds were higher for the larger droplet.

droplet mergers. 2.5 μl droplets were split in a 125 μm channel gap at various voltages, according to the pattern shown in figure 7(a). Experiments indicate that the threshold voltage to split droplets is 450 V, which corresponds to a threshold electric field of 3.6 V μm^{-1}. The splitting time decreased at higher voltages (figure 7(b)).

3.3. Understanding EW-induced droplet generation from an open reservoir

In an EHP condenser, liquid must be imbibed from an open channel into a two-plate configuration, and then split into discrete drops for transportation. This section provides a theoretical framework for droplet generation, since generation from an open-to-air reservoir has not been previously studied. The starting point for this analysis is the pressure difference across a liquid–gas interface as a function of the curvature (Guan *et al* 2016):

$$\Delta P = \gamma_{lv}\left(\frac{1}{R_{xy}} + \frac{1}{R_z}\right) \tag{1}$$

where R is the radius of curvature (figure 8(a)). The radius of curvature in the z-direction (R_z) can be expressed in terms of the contact angle of the droplet on the top and bottom surfaces as Cho *et al* (2003):

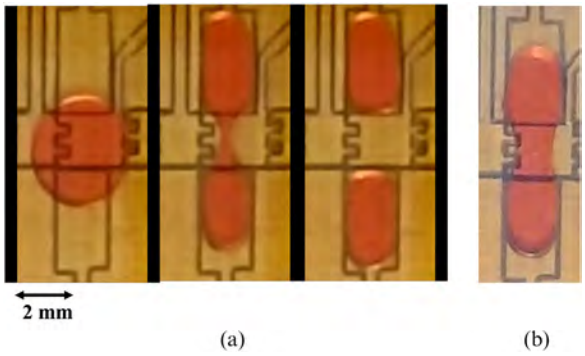

Figure 6. Splitting a droplet from 2 × 2.5 mm center electrode onto 2 × 4 mm side electrodes. (a) 6 μl droplet in a 375 μm channel gap splits completely, (b) 8 μl droplet in a 500 μm channel gap necks but does not split.

$$R_z = -\frac{h}{(\cos\theta_t + \cos\theta_b)} \tag{2}$$

where h is the channel gap. This z-direction curvature is seen in figure 8(b), which shows a side view schematic of a droplet in mid-motion between an activated electrode and a non-activated electrode. $\theta_{b,off}$ is the contact angle on the bottom surface under no voltage, $\theta_{b,on}$ is the contact angle under an applied voltage, and θ_t is the contact angle on the top surface. It is noted that $\theta_t = \theta_{b,off}$, if the same hydrophobic layer is used for the top and bottom surfaces. It is also noted that the curvature in the x-y direction changes during droplet generation.

During droplet generation from a covered reservoir, a liquid finger is drawn underneath the cover plate from the bulk liquid; subsequently the electrodes in the middle of the finger are deactivated to enable pinch-off. Depending on the pinch-off location, liquid can flow into the newly generated droplet or back into the bulk liquid (Fair 2007). The key to successful droplet generation is maintaining a positive pressure gradient ($P_2 > P_1$) from the necking site to the reservoir until pinching is achieved (Fair 2007). For a covered reservoir, the pressure difference between the necking site and the reservoir can be estimated using equations (1) and (2) as:

$$\Delta P_{21,\text{covered}} = \gamma_{lv}\left(\frac{1}{R_{2,xy}} - \frac{1}{R_{1,xy}} - \frac{(\cos\theta_{b,off} - \cos\theta_{b,on})}{h}\right). \tag{3}$$

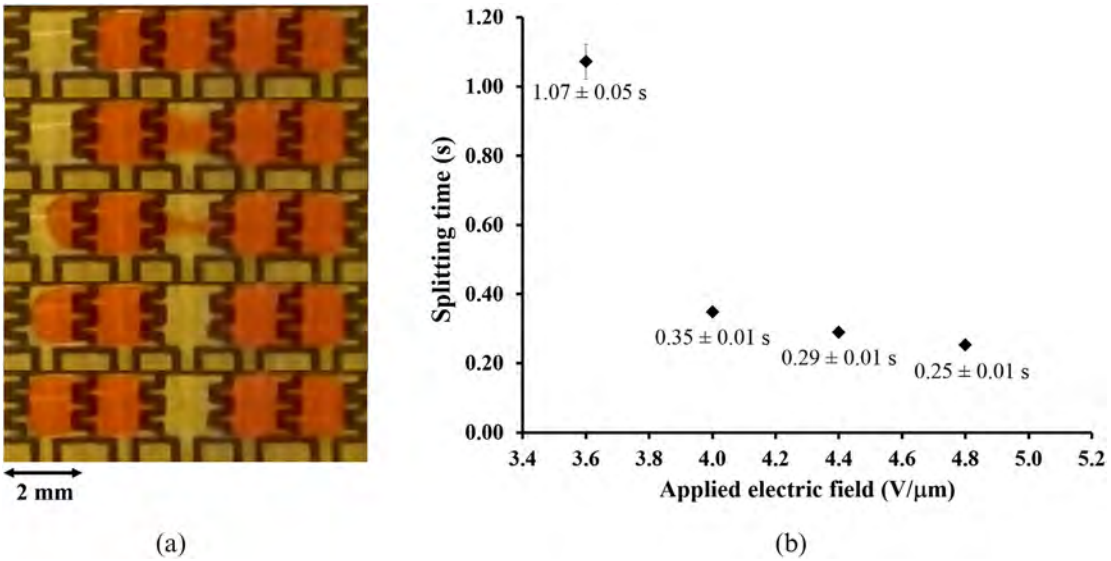

Figure 7. (a) Sequence of steps involved in splitting 2.5 μl droplets in a 125 μm channel gap. (b) Dependence of the splitting time on the electric field.

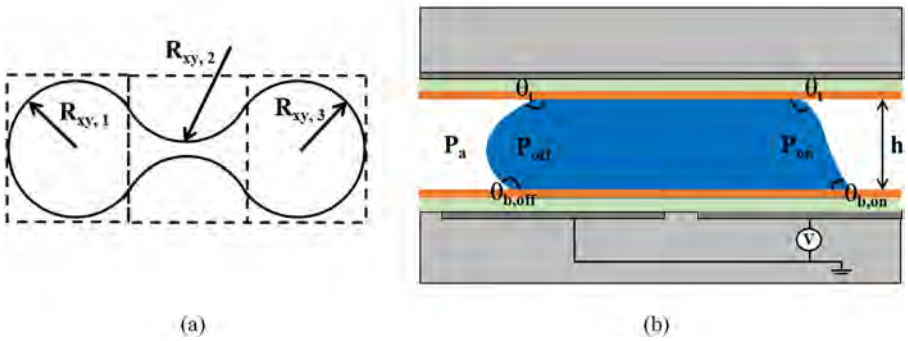

Figure 8. (a) Schematic illustration of droplet generation by breaking off the liquid neck to form a droplet of radius R_3 from a reservoir of radius R_1. (b) Side view schematic of a droplet in mid-motion between a ground electrode and an active electrode.

Pinching occurs when R_2 reaches the critical point, where the two sides of the neck meet. Assuming square electrodes, the critical R_2 needed for splitting can be approximated in terms of the number of electrodes in the pinch-off region (N) and the radius of curvature in the creation region (R_3) (Fair 2007) as:

$$|R_{2,\,\text{critical}}| \approx (N^2 + 1)R_3/2. \tag{4}$$

Once the critical R_2 is fixed by the system geometry, the pressure relationship is only modified by the channel gap and electrode voltages. A large critical radius (R_2) and small channel gap (h) are advantageous for pinch-off. The critical radius (R_2) will increase with increasing number of displacement electrodes (N). Another way to maintain a positive pressure gradient until pinch-off is to activate the electrode underneath the reservoir.

The above analysis for a covered reservoir can be extended to droplet pinching from an open-to-air reservoir by assuming the droplet outside the plates as a truncated sphere (figure 9).

The volume, V_d, height, H, and base radius, a, of a droplet modeled as a spherical cap can be expressed as:

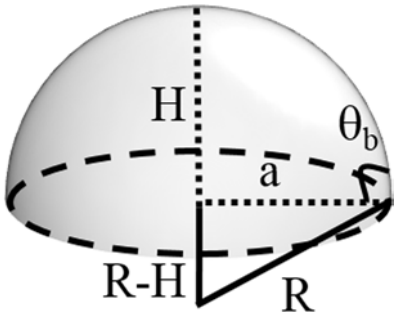

Figure 9. Representation of a droplet as a truncated sphere in the open-to-air reservoir.

$$V_\text{d} = \frac{1}{3}\pi R^3(2 - 3\cos\theta_\text{b} + \cos^3\theta_\text{b}) \tag{5}$$

$$H = R(1 - \cos\theta_\text{b}); \quad a = \sqrt{H(2R - H)}. \tag{6}$$

R_{xy} and R_z for the spherical cap can be estimated from equation (5). Because the spherical cap is symmetrical in this example, $R_{xy} = R_z$ and can be represented simply by a new variable, R_1. The pressure gradient then becomes:

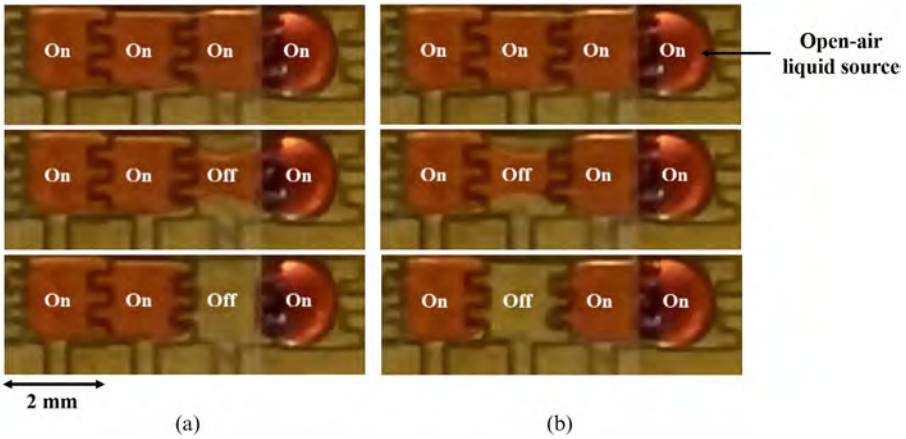

Figure 10. Sequence of images showing droplet generation from an open-to-air reservoir in a 125 μm channel. The location of the deactivated electrode controlled final droplet lengths of (a) 4 mm and (b) 2 mm. The electrode size was 2 × 2 mm and the droplet volume was 6 μl.

$$\Delta P_{21,\text{open}} = \gamma_{lv}\left(\frac{1}{R_{2,xy}} - \frac{1}{R_1} - \frac{(\cos\theta_{\text{b,off}} + \cos\theta_t)}{h} - \frac{1}{R_1}\right). \tag{7}$$

Equation (7) shows that a small channel gap, large electrode size, and large bulk droplet size are advantageous for pinch-off. In addition, a large reservoir pool increases R_1 and raises the pressure gradient even further. However, one notable difference from a covered reservoir system is that for an open system, it is not required to activate the electrode underneath the reservoir if $(\cos\theta_{\text{b,off}} + \cos\theta_t)/h$ is sufficiently large. It is noted that this model does not include contact angle hysteresis, which can retard fluid motion. While analysis of hysteresis is important to predict the precise motion of three phase lines, the present work targets a first-principles-based conceptual understanding of droplet generation from open-to-air reservoirs, and hysteresis-related complexities are not discussed.

3.4. Experiments on droplet generation from an open-to-air reservoir

Following the analytical framework of the previous section, this section details experimental studies of droplet generation from an open-to-air reservoir. Since the heat transport capacity of the EHP is linearly related to the channel gap, the objective was to estimate the maximum channel gap that would be able to draw in liquid and pinch it to create droplets. It is noted that these studies are different from those in section 3.2, which involved symmetric splitting of droplets. The experiments in this section simulate droplet generation (asymmetric splitting from a reservoir of fluid) as depicted in figure 1. Experiments were conducted to generate droplets in channel gaps of 125 μm, 250 μm, 375 μm and 500 μm. For a 125 μm channel gap, the pressure difference between the deactivated electrode and the bulk liquid easily created a negative curvature and pinched a discrete droplet off. Varying the location of the deactivated electrode created droplets of different lengths and volumes as shown in figure 10 and video 5. Continuous generation of droplets followed by movement away from the pinching site is captured in video 6. Despite the bulk liquid volume decreasing with time, the pressure gradient remained high enough for pinching until the volume was completely depleted. It is noted that the pinching speed was sensitive to surface imperfections and contact line friction.

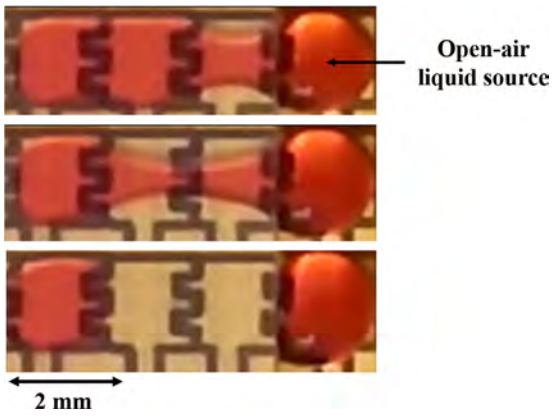

Figure 11. Sequence of images showing droplet generation from an open-to-air reservoir in a 250 μm channel. Droplet generation requires deactivating two central electrodes, instead of the one electrode requirement at lower channel gaps. The electrode size was 2 × 2 mm and the droplet volume was 6 μl.

This study also targets the identification of electrode configurations that would enable droplet generation at high channel gaps. High channel gaps decrease the internal pressure gradient, but equation (4) shows that increasing the number of deactivated electrodes can counteract this effect. Repeated and successful droplet generation in a 250 μm channel gap was successful with two electrodes deactivated, instead of one, which creates a longer tail before pinch-off (figure 11 and video 7). It is important to note that droplets could not be generated for channel gaps of 375 μm and 500 μm, since the necking was not strong enough to achieve splitting.

4. Discussion—implications of present work on performance parameters of the EHP

This section assesses the impact of the present study on the design and estimated performance of an EHP. The most important finding of this study is that the maximum channel gap that allows droplet movement, droplet splitting and droplet

Table 2. Comparison of significant parameters of the current design of the EHP and a previous conceptual design (Hale and Bahadur 2015).

Parameter	EHP design from Hale and Bahadur (2015)	EHP design based on current work
Adiabatic length	1 m	1 m
Evaporator length	5 cm	5 cm
Condenser length	5 cm	5 cm
Total width	10 cm	10 cm
Total height	4 mm	4 mm
Liquid channel height	0.75 mm	0.125 mm
Liquid channel width	1.25 mm	2.00 mm
Vapor channel height	3.00 mm	2.625 mm
Vapor channel width	8.25 mm	100 mm
Channel wall thickness	0.25 mm	0.25 mm
Droplet volume	1.2 μl	1.5 μl
Electrode size	1.25 $\times$ 0.5 mm	2 $\times$ 2 mm
Heat pipe wall thickness	0.5 mm	0.5 mm
Number of liquid channels	10	44
Heat transfer capacity	1510 W	1650 W
Thermal resistance	0.01 K W^{-1}	0.01 K W^{-1}

generation (from an open-to-air reservoir) is 250 μm. A conservative estimate for enhanced reliability and repeatability of these microfluidic operations will be 125 μm. The previous conceptual architecture of the EHP by Hale and Bahadur (2015) assumed a higher channel gap of 0.75 mm. Accordingly, it would appear that the heat transport capacity will be much less than 1.5 kW, as estimated by Hale and Bahadur (2015). Although a decreased channel gap reduces the droplet volume, reorienting the liquid and vapor channels from the conceptual design of Hale and Bahadur (2015) can counteract the effect of smaller channel gaps. Instead of the alternate liquid and vapor channel arrangement of the previous design, the vapor can return in one large channel on the top of the EHP, leaving a much larger area for liquid channels on the bottom part of the EHP (figure 1(a)). Furthermore, this study indicates that larger electrode sizes (2 $\times$ 2 mm, as opposed to the earlier considered size of 1.25 $\times$ 0.5 mm) can successfully transport droplets, which increases the liquid loading per unit footprint area of the EHP. The net effect of all these changes is that the number of liquid channels increases to 44 (from 10 in the previous study), even while the droplet volume decreases due to the smaller channel gap. The heat transport capacity of a 10 cm wide $\times$ 4 mm high $\times$ 1 m long EHP increases to 1650 W, compared to the previous estimate of 1510 W. The heat transport capacity Q is estimated from the condensate mass flow rate ($\dot{m}$) and the latent heat of vaporization h_{fg} as $Q = \dot{m}h_{fg}$. The thermal resistance does not change significantly, and is 0.01 K W^{-1}. Table 2 compares the significant parameters of the current and the previous designs. The new design, which is based on experimentally validated microfluidic operations, will offer the significant advantages over competing heat movement technologies outlined in the studies of Hale and Bahadur (2015) and Hale and Bahadur (2016).

5. Conclusions

This work studies the fundamental microfluidic operations underlying an EHP using devices manufactured via a rapid, scalable technique. The dielectric layer is one of the most critical factors in EW systems; the present technique uses a thick, pinhole free dielectric layer, which drives up the operating voltages, but will substantially reduce failures related to the dielectric layer. Key components of this technique (i.e. PCB as substrate, mechanically milled electrodes, removable and pinhole-free dielectric layer) can be applied to the development of other EW-based platforms as well. Experiments reveal that the microfluidic operations of droplet pumping, droplet splitting, and droplet generation (from an open reservoir) can be successfully conducted at channel gaps up to 1 mm, 375 μm and 250 μm, respectively. Droplet generation considerations thus restrict the maximum channel gap to 250 μm. The channel gap is a key parameter which determines the heat transport capacity and the cross-section footprint of the EHP. The present experiments report droplet speeds of up to 10.5 mm s^{-1} in a two-plate configuration, which is higher than previously reported values on similar rapid-manufactured EW platforms. Overall, this work provides a manufacturing tool and a scientific basis for further development of the EHP.

Acknowledgments

This material is based upon work partly supported by the National Science Foundation Division of Chemical, Bioengineering, Environmental, and Transport Systems under Grant No. NSF-1605789 and NSF-1653412.

References

Abdelgawad M and Wheeler A 2007 Rapid prototyping in copper substrates for digital microfluidics *Adv. Mater.* **19** 133–7

Abdelgawad M and Wheeler A 2008 Low-cost, rapid-prototyping of digital microfluidic devices *Microfluid. Nanofluid.* **4** 349–55

Bahadur V and Garimella S V 2006 An energy-based model for electrowetting-induced droplet motion *J. Micromech. Microeng.* **16** 1494–503

Bahadur V and Garimella S V 2008 Electrowetting-based control of droplet transition and morphology on artificially microstructured surfaces *Langmuir* **24** 8338–45

Baird E and Mohseni E B 2008 Digitized heat transfer: a new paradigm for thermal management of compact micro systems *IEEE Trans. Compon. Packag. Manuf. Technol.* **31** 143–51

Chen L and Bonaccurso E 2014 Electrowetting—from statics to dynamics *Adv. Colloid Interface Sci.* **210** 2–12

Cheng J and Chen C-L 2012 Spot cooling using electrowetting-controlled thin film heat transfer *Proc. ASME Micro/Nanoscale Heat Mass Transfer Int. Conf.* pp 275–81

Cho S K, Fan S-K, Moon H and Kim C J 2002 Towards digital microfluidic circuits: creating, transporting, cutting and

merging liquid droplets by electrowetting-based acutation *IEEE Conf. on Micro Electro Mechanical Systems* pp 32–5
Cho S K, Moon H and Kim C J 2003 Creating, transporting, cutting, and merging liquid droplets by electrowetting-based actuation for digital microfluidic circuits *J. Microelectromech. Syst.* **12** 69–80
Choi K, Ng A H, Fobel R and Wheeler A R 2012 Digital microfluidics *Annu. Rev. Anal. Chem.* **5** 413–40
Ding H, Sadeghi S, Shah G J, Chen S, Keng P Y, Kim C J and van Dam R M 2012 Accurate dispensing of volatile reagents on demand for chemical reactions in EWOD chips *Lab Chip* **12** 3331–40
Faghri A 1995 *Heat Pipe Science and Technology* (Boca Raton, FL: CRC Press)
Fair R 2007 Digital microfluidics: is a true lab-on-a-chip possible? *Microfluid. Nanofluid.* **3** 245–81
Foat T G *et al* 2016 A prototype personal aerosol sampler based on electrostatic precipitation and electrowetting-on-dielectric actuation of droplets *J. Aerosol Sci.* **95** 43–53
Gong J and Kim C 2008 All-electronic droplet generation on-chip with real-time feedback control for EWOD digital microfluidics *Lab Chip* **8** 898–906
Guan Y, Tong A, Jagath N, Nikapitiya B and Moon H 2016 Numerical modeling of microscale droplet dispensing in parallel-plate electrowetting-on-dielectric (EWOD) devices with various reservoir designs *Microfluid. Nanofluid.* **20** 39
Gupta R, Sheth D, Boone T, Sevilla A and Frechette J 2011 Impact of pinning of the triple contact line on electrowetting performance *Langmuir* **27** 14923–9
Hale R S and Bahadur V 2015 Electrowetting heat pipes for heat transport over extended distances *IEEE Trans. Compon. Packag. Manuf. Technol.* **5** 1441–50
Hale R S and Bahadur V 2016 Performance comparison of electrowetting heat pipe for extended distance heat transport *IEEE Conf. on Thermal and Thermomechanical Phenomena in Electronic Systems (ITHERM)* pp 1013–8
Hayes R and Feenstra B J 2003 Video-speed electronic paper based on electrowetting *Nature* **425** 383–5
Heikenfeld J, Drzaic P, Yeo J-S and Koch T 2011 Review paper: a critical review of the present and future prospects for electronic paper *J. Soc. Inf. Disp.* **19** 129–56
Hong J, Lee S J, Koo B C, Suh Y K and Kang K H 2012 Size-selective sliding of sessile drops on a slightly inclined plane using low-frequency AC electrowetting *Langmuir* **28** 6307–12
Hong J, Park J K, Koo B, Kang K H and Suh Y K 2013 Drop transport between two non-parallel plates via AC electrowetting-driven oscillation *Sensors Actuators* B **188** 637–43
Jain V, Raj T, Deshmukh R and Patrikar R 2015 Design, fabriaction and characterization of low cost printed circuit board based EWOD device for digital microfluidics *Microsyst. Technol.* **23** 1–9
Jang L-S, Hsu C-Y and Chen C-H 2009 Effect of electrode geometry on performance of EWOD device driven by battery-based system *Biomed. Microdevices* **11** 1029–36
Jebrail M, Bartsch M and Patel K 2012 Digital microfluidics: a versatile tool for applications in chemistry, biology and medicine *Lab Chip* **12** 2452–63
Kumari N, Bahadur V and Garimella S V 2008 Electrical actuation of electrically conducting droplets using AC and DC voltages *J. Micromech. Microeng.* **18** 105015
Kumari N and Garimella S V 2011 Characterization of the heat transfer accompanying electrowetting or gravity-induced droplet motion *Int. J. Heat Mass Transfer* **54** 4037–50
Lee J, Moon H, Fowler J, Schoellhammer T and Kim C J 2002 Electrowetting and electrowetting-on-dielectric for microscale liquid handling *Sensors Acutators* A **95** 259–68
Leiterer C, Urban M, Fritzsche W, Goldys E and Inglis D 2015 Printed circuit board as platform for disposable lab-on-a-chip applications *Proc. SPIE* **9668** 96680X
Li Y, Chen R and Baker R 2014 A fast fabricating electro-wetting platform to implement large droplet manipulation *IEEE Int. Midwest Symp. on Circuits and Systems* pp 326–329
Liu Y, Banerjee A and Papautsky I 2014 Precise droplet volume measurement and electrode-based volume metering in digital microfluidics *Microfluid. Nanofluid.* **17** 295–303
McHale G, Brown C V and Sampara N 2013 Voltage-induced spreading and superspreading of liquids *Nat. Commun.* **4** 1605
Migliaccio C P and Garimella S V 2013 Evaporative heat transfer from an electrowetted ribbon a heated substrate *Int. J. Heat Mass Transfer* **57** 73–81
Mohseni K and Baird E 2007 Digitized heat transfer using electrowetting on dielectric *Nanoscale Microscale Therm.* **11** 99–108
Mugele F and Baret J-C 2005 Electrowetting: from basics to applications *J Phys: Condens Matter* **17** R705–74
Nelson W and Kim C 2012 Droplet acutation by electrowetting-on-dielectric (EWOD): a review *J. Adhesion Sci. Technol.* **26** 1747–71
Pamula V K and Chakrabarty K 2003 Cooling of integrated circuits using droplet-based microfluidics *Proc. GLSVLSI* pp 84–87
Pan M, Kim M, Kuiper S and Tang S 2015 Actuating fluid-fluid interfaces for the reconfiguration of light *IEEE J. Sel. Top. Quantum Eletron.* **21** 9100612
Park J K, Lee S J and Kang K H 2009 A new switching method of two-dimensional ewod-based droplet translation on single-plate configuration *Proc. ASME ICNMM* 82272
Peng C, Zhang Z, Kim C J and Ju Y S 2014 EWOD (electrowetting on dielectric) digital microfluidics powered by finger actuation *Lab Chip* **14** 1117–22
Phongsomboon C, Sukhthang K, Wechsatol W, Tuantranont A and Lomas T 2011 Droplet movement on a low cost EWOD according to applied frequencies and voltages *Appl. Mech. Mater.* **87** 140–5
Pollack M, Shenderov A and Fair R 2002 Electrowetting-based actuation of droplets for integrated microfluidics *Lab Chip* **2** 96–101
Quilliet C and Berge B 2001 Electrowetting: a recent outbreak *Curr. Opin. Colloid Interface Sci.* **6** 34–9
Ren H, Fair R and Pollack M 2004 Automated on-chip droplet dispensing with volume control by electro-wetting actuation and capacitance metering *Sensors Actuators* B **98** 319–27
Russell A, Kreit E and Heikenfeld J 2014 Scaling dielectrowetting optical shutters to higher resolution: microfluidic and optical implications *Langmuir* **30** 5357–62
SadAbadi H, Stiharu I, Packirisamy M and Wuthrich R 2009 A parametric study of interdigital electrodes for achieving high droplet speed in electrowetting *IEEE Proc. of Microsystems and Nanoelectronics Research Conf.* pp 76–9
Samiei E and Hoorfar M 2015 Systematic analysis of geometrical based unequal droplet splitting in digital microfluidics *J. Micromech. Microeng.* **25** 055008
Shahriari A, Hermes M and Bahadur V 2016 Electrical control and enhancement of boiling heat transfer during quenching *Appl. Phys. Lett.* **108** 091607
Shih S, Fobel R, Kumar P and Wheeler A 2011 A feedback control system for high-fidelity digital microfluidics *Lab Chip* **11** 535–40
Walker S and Shapiro B 2006 Modeling the fluid dynamics of electrowetting on dielectric *J. Microelectromech. Sys.* **15** 986–1000
Wang W, Jones T and Harding D 2011 On-chip double emulsion droplet assembly using electrowetting-on-dielectric and dielectrophoresis *Fusion Sci. Technol.* **59** 240–9
You H and Steckl A J 2010 Three-color electrowetting display device for electronic paper *Appl. Phys. Lett.* **97** 023514
Zhou K, Heikenfeld J, Dean K A, Howard E M and Johnson M R 2009 A full description of a simple and scalable fabrication process for electrowetting displays *J. Micromech. Microeng.* **19** 065029